

Fabricated HMNPs with Size Approaching ~100 nm for MMC Loading and Sustained-release, as well as Labeling $^{99}\text{Tc}^{\text{m}}$

Yuxiang Yang (✉ yxyang@ecust.edu.cn)

East China University of Science and Technology <https://orcid.org/0000-0003-1836-1341>

Ziling Chang

East China University of Science & Technology, Shanghai

Mengyang Dong

East China University of Science & Technology, Shanghai

Huafei Li

Shanghai University

Chaoying Ni

University of Delaware

Hongming Yuan

Jilin University

Research Article

Keywords: hollow magnetic nano-spheres, particle size, mitomycin C, sustained-release, targeting label

Posted Date: March 22nd, 2022

DOI: <https://doi.org/10.21203/rs.3.rs-1450677/v1>

License:   This work is licensed under a Creative Commons Attribution 4.0 International License.

[Read Full License](#)

Abstract

Herein, we developed the dual-function template method to fabricate hollow magnetic nano-spheres (denoted as HMNPs-C_n, n = 16, 18) with a mesoporous shell and hollow interior structure using alkyl chain trimethoxysilane templating. The microstructure of the HMNPs-C_n was investigated by means of XRD, FT-IR, EDS, SEM, TEM and N₂-BET analyses. The shorter chain template directed formation of HMNPs-C₁₆ with size of 119 nm, having disordered inkbottle type mesopores and saturation magnetization of 50.01 emu/g. It can be observed that, mitomycin C (MMC) loaded HMNPs-C_n hollow spheres showed a clear pH-dependent drug release behavior, having a higher release rate in acidic environments of pH 5.7. For the pH 5.7 and 7.4 release, the diffusion through HMNPs-C_n hollow spheres is the rate limiting step, the release kinetic for HMNPs-C₁₆-MMC composites follows pseudo-first-order attributable to its special pore structure. For this reason the inner cavity of HMNPs-C₁₆ could be labeled with radioisotope ⁹⁹Tc^m to study the magnetic targeting distribution of HMNPs-C₁₆ in vivo, and its cytotoxicity against in vitro HeLa cells was also studied. These results indicate the potential of HMNPs-C₁₆ in the magnetic targeted drug delivery system.

1. Introduction

MMC is a class of antibiotics for cancer whose chemical structure has three active groups of quinone, acetyl imide and ammonium carbamate. Its action is similar to that of an alkylating agent, forming cross-linking with the DNA chain and inhibiting DNA replication. MMC has an obvious antitumor effect, but its side effects are serious [1–3]. Delivery through the carrier can increase the potency of the drug and reduce side effects. Many studies have used magnetic nanomaterials loaded with MMC to achieve targeted drug delivery. Zhu et al. [4] synthesized magnetic nanoparticles with albumin as the carrier material, though the MMC loading was only 6%. M. Eizadi Sharifabad et al. [5] carried out the coprecipitation method and following self-assembled lipid tubules as templates to obtain liposome silicon coated 10 nm magnetic core, while the highest MMC loading only reached at 7 μg/mg. Li et al. [6] synthesized mPEG-PLA diblock copolymer conjugate by ring-opening polymerization of L-lactide using stannous acid as a catalysis, the drug loading in micelles of copolymer conjugate ranged from 11.23–20.01%. It seems the copolymer conjugate is promising material to load MMC, though there still exists some drawbacks, such as complex synthesis and multiple fabrication process, as well as low load of MMC.

Mesoporous silica has been widely studied as a drug carrier because of its advantages of it being non-toxic, having tunable pore size and high surface area [7, 8]. However, mesoporous silica as a drug carrier has some limitations, such as the inability to deliver drugs directly to organ and site specific tumors, and it ineffectively being used for regional target therapy, especially since anticancer drugs have the ability to damage normal cells [9–11]. In order to promote therapeutic efficiency and avoid damage caused by drug toxicity in normal cells, the integration of mesoporous silica with nano-magnetic materials can indeed achieve this goal by introducing drugs into tumor target cells. Generally speaking, there are three ways to

perform the integration of mesoporous silica with magnetic materials: preparation of magnetic silicon spheres with core-shell structure [12, 13], magnetic material encapsulated in the mesoporous silica pore [14], and fabrication of hollow magnetic nanoparticles with a mesoporous shell and hollow interior structure [15]. The as expected magnetic materials fabricated by the first two methods have low drug loading rate. In comparison, the HMNPs based on the third option can provide more drug loading and act as an efficient magnetic drug delivery system on account of its large internal space and high saturation magnetization, consequently making HMNPs nanomaterials very attractive in biomedical application.

So far, there are many methods utilized to fabricate hollow magnetic nanoparticles. Zhang et al. [16] fabricated CTAB/silicate composite micelles to pack the surrounding fluorocarbon surfactant (FC 4) vesicles with entrapped Fe_3O_4 nanoparticles via a S^+I^- self-assembly pathway. Although the obtained HMNPs exhibits small particle size, high surface area, large pore volume and most importantly a high saturation magnetization value, the sample present non-uniform size distribution, is unfavorable to biomedical application. As such, people began to turn to exploring the construction of HMNPs via the facile hard template-directed ordered assembly approach. Junjie Yuan et al. [17] prepared HMNPs via depositing magnetic particles (Fe_3O_4) on the surface of sulfonated hollow silica spheres, though it is difficult to obtain well-dispersed magnetic hollow silica spheres, as a result of hard to control coprecipitation of Fe_3O_4 on the surface. Zhu et al. [18] prepared rattle-type magnetic hollow spheres with carbon spheres as templates, exhibiting large particle size, but low saturation magnetization value. With the nanosized CaCO_3 as a hard template, the nanosized $\text{Fe}_3\text{O}_4/\text{CaCO}_3$ can be trapped into the mesoporous silica during the sol-gel process [19]. By means of acid dissolution, magnetic hollow spheres with a diameter of 60–90 nm can be obtained—but with low saturation magnetization value—and its drug-load amount did not exceed 15%. Therefore, the feasible fabrication of a novel kind of magnetic core/mesoporous silica shell nanospheres with a uniform particle size and high saturation magnetization value is urgently needed.

At present, a new method to fabricate HMNPs by trapping core-shell $\text{Fe}_2\text{O}_3/\text{SiO}_2$ nanoparticles into mesoporous silica with surfactant octadecyltrimethoxysilane (C_{18}TMS) acting both as a template and silica source has been put forward [20]. The most obvious advantage of the dual-function template method is its ability to avoid the formation of a non-uniform mesoporous silica shell and obtain uniformly size-distributed magnetic nanoparticles with high saturation magnetization value. However, drug carriers with a diameter of ~ 100 nm are more effective for chemotherapy and gene delivery [21] — they are capable of penetrating the blood–brain barrier and the blood-testis barrier, have rapid distribution to the body, while also not affecting the function of organs.

So we propose our query, whether to adjust the chain length of dual-function template to obtain HMNPs with diameter approaching ~ 100 nm and high saturation magnetization value. Our previous work perhaps supports our idea, owing to the fact that [22] the chain length is an important chemical factor: the longer facilitates the formation of millimeter-scaled silica ropes, while the shorter leads to the formation of micrometer-scaled rope fibers of mesoporous silica with 2D hexagonal structure.

The dual-function template of hexadecyltrimethoxysilane (C_{16} TMS) with shorter chain length in place of surfactant octadecyltrimethoxysilane (C_{18} TMS) was used to fabricate HMNPs with diameter approaching ~ 100 nm. As a consequence of the large hollow cavity space and high saturation magnetization value, we also performed MMC loading and releasing on MMC-loaded HMNPs, as well as $^{99}\text{Tc}^m$ labeled HMNPs, to study magnetic targeting distribution in vivo.

2. Experimental

2.1. Materials

Iron (III) chloride hexahydrate, hydrochloric acid, iso-Propyl alcohol, ammonium hydroxide, tetraethyl orthosilicate, and ethanol (all of analytical grade) were purchased from Shanghai Sinopharm Chemical Reagent Co., Ltd. (Shanghai, China). Hexadecyltrimethoxysilane and octadecyltrimethoxysilane were purchased from Aladdin industrial Corporation (Shanghai, China). Mitomycin C was purchased from Hubei Honch Pharmaceutical Co., Ltd. Pertechnetate ($^{99}\text{Tc}^m$) Sodium injection was purchased from Shanghai Atom Kexing Pharmaceutical Co., Ltd.

2.2. Synthesis strategy and formation mechanism of the approach

The hollow magnetic nano-spheres can be obtained by using either sacrificial templates in the core area or selective etching inner layer of silica [17], the surfactant C_n TMS here is a dual-function agent for both the stabilization of hematite core and mesoporous directing template, and the resulted structure can be either strict hematite/MSN core/shell or hematite embedded in MSN framework in a scattered manner. An assembly route to synthesize of HMNPs can be described as shown in Fig. 1.

First, the silica is closely coated on the core of hematite ($\alpha\text{-Fe}_2\text{O}_3$), the active trimethoxysilane of the part surfactant C_n TMS then reacts with hydroxyl groups of the silica surface coated on the hematite core to form hydrophobic micellar-type of the clusters around $\text{Fe}_2\text{O}_3@SiO_2$. Third, hydrophobic alkyl chains part of (C_{16} - C_{18} alkyl) trimethoxysilane are inserted into hydrophobic micelle according to the principle of minimum energy [31], and the TEOS assembles into ordered mesoporous silica directed by the C_{16} - C_{18} alkyl chain, while active trimethoxysilane of inserted C_n TMS hydrolyzes into oligomeric silica species inside the palisade layer between alkyl chains, and an end capping self-assembly of mesoporous silica surround $\text{Fe}_2\text{O}_3@SiO_2$. Finally, through the next process of hydrothermal, calcination and hydrogen reductions, the HMNPs can be obtained. From Fig. 1, it can be observed that the size of HMNPs is based on the chain length of C_n TMS. When the C_{18} alkyl chain is replaced by C_{16} alkyl chain, the obtained HMNPs certainly shows a smaller size.

2.3. Synthesis of Silica-Coated Magnetite Nanoparticle ($\text{Fe}_2\text{O}_3@SiO_2$).

First, uniform hematite $\alpha\text{-Fe}_2\text{O}_3$ were obtained by refluxing a 50 mL solution containing $0.02 \text{ mol}\cdot\text{mL}^{-1}$ $\text{FeCl}_3\cdot 6\text{H}_2\text{O}$ and $1\times 10^{-3} \text{ mol}\cdot\text{mL}^{-1}$ HCl at 100°C for 24h. Afterwards, 50 mg of the dry $\alpha\text{-Fe}_2\text{O}_3$ nanoparticles were ultrasonically dispersed in 40 mL of boiled deionized water, 200 mL of isopropyl alcohol and 6 mL of NH_3 ; 0.15 mL of TEOS was then added under vigorous stirring in turn at regular intervals. After continuous stirring for 8 h at 25°C , the resulting mixture was centrifuged to wash away uncoated silica, the obtained $\text{Fe}_2\text{O}_3@\text{SiO}_2$ sample was ultrasonically dispersed in 5 mL ethanol to form stock solution A, and preserved in a refrigerator at 4°C for further use.

2.4. Preparation of $\alpha\text{-Fe}_2\text{O}_3@\text{SiO}_2@m\text{SiO}_2\text{-C}_n$ ($n = 16, 18$)

All stock solution A was added into a solution containing 2 mL of boiled deionized water, 10 mL of 95% ethanol, 0.72 mL of NH_3 , and 0.3 mL of $\text{C}_{16}\text{TMS/TEOS}$ mixture, with the $\text{C}_{16}\text{TMS/TEOS}$ volume ratio of 1:2.47 was then added under vigorous stirring in turn at regular intervals. After reaction for 6 h at 25°C , the $\alpha\text{-Fe}_2\text{O}_3@\text{SiO}_2@m\text{SiO}_2\text{-C}_{16}$ were recovered by centrifugation, washed with ethanol, and dried.

The preparation of $\alpha\text{-Fe}_2\text{O}_3@\text{SiO}_2@m\text{SiO}_2\text{-C}_{18}$ was carried out by using $\text{C}_{18}\text{TMS/TEOS}$ as substitutes for the $\text{C}_{16}\text{TMS/TEOS}$ with the unchanged volume ratio of 1:2.47, while keeping all other parameters fixed.

2.5. Synthesis of hollow magnetic nanoparticles (HMNPs- C_n)

The hydrothermal method was employed to prepare a hollow structure, the obtained $\alpha\text{-Fe}_2\text{O}_3@\text{SiO}_2@m\text{SiO}_2\text{-C}_n$ ($n = 16, 18$) was dispersed in a mixture of 28 mL boiled deionized water and 2 mL ethanol. The resulting solution was transferred into a 50 mL Teflon-lined autoclave, and the hydrothermal synthesis was carried out at 130°C for 20 h. After centrifugal separating and being washed with ethanol, the obtained product was vacuum dried for approximately 6 hours, and calcined in the tube furnace under a nitrogen atmosphere at 550°C for 6 h to form an outer mesopore channel.

The hollow interior structure was obtained by selectively etching away the internal homogeneous silica core of $\alpha\text{-Fe}_2\text{O}_3@\text{SiO}_2@m\text{SiO}_2\text{-C}_n$. Thus the calcined product was etched for 3 h in a flow of reducing H_2 (4 vol%)/ N_2 gas at atmospheric pressure and a temperature of approximately 400°C . The obtained product was named HMNPs- C_n ($n = 16, 18$).

2.6. Loading and sustained-release of Mitomycin C

2.6.1 Standard curve of Mitomycin C

MMC standard stock solution of $100 \mu\text{g/mL}$ was prepared as follows. 10.0 mg MMC was ultrasonically dissolved in 50 mL of boiled deionized water, and quantitatively transferred to a 100 ml volumetric flask, then be diluted to the mark with boiled deionized water. Diluted MMC standard solutions of $0.5 \sim 20.0 \mu\text{g/mL}$ were made by diluting $0.5 \sim 20.0 \text{ mL}$ of MMC stock solution to 100 ml respectively.

The measurement of free MMC content in the solution was carried out using SHIMADZU UV-VIS Spectrophotometers UV-2600. As shown in Fig. 2a, UV-vis spectrum of the MMC solution revealed two apparent broad peak wavelengths at 214 nm and 360 nm respectively, within ranges of 150 ~ 500 nm (Fig. 2a); the maximum absorption peak was at the wavelength of 360 nm. The absorbance at 360 nm was therefore used to determine the loading. The ultraviolet absorption of MMC at a wavelength of 360 nm was directly proportional to the concentration of the MMC, and thus the standard curve was plotted by the absorbance recorded at 360 nm versus the concentration of the MMC (C, $\mu\text{g}/\text{mL}$) to determine the MMC concentration. Hence, the readout at 360 nm was compared with standard curve to calculate the unloaded MMC concentration. The assay mixture usually contained 0.5 ~ 20.0 $\mu\text{g}/\text{mL}$ MMC in boiled deionized water in a total volume of 3 mL.

2.6.2 MMC loading and sustained release

0.050 g, 0.075 g, 0.100 g, 0.150 g and 0.200 g of MMC were separately added into 5 mL of n-hexane solution with 0.20 g HMNPs- C_n ($n = 16, 18$), treated under ultrasound for 30 min, and stirred for 12 h. The mixture within the vessel was then placed in a temperature controlled shaking incubator (model: TQZ-312) at a speed of 150 rpm and kept at 37°C for 24 h. Finally, the resulting MMC loaded HMNPs- C_n was magnetically separated, followed by washing in anhydrous n-hexane, and then vacuum dried at 30°C. The supernatant liquid and washed solution were collected to measure the amount of free MMC, while the MMC loaded HMNPs nanoparticles were kept for the next release determination.

The MMC loading efficiency and drug loading content were calculated using the following equation:

$$\text{Loading efficiency} = (W_{\text{total drug}} - W_{\text{drug in supernatant}}) / W_{\text{total drug}} \times 100$$

The release of the MMC was carried out by distributing the above obtained MMC loaded HMNPs- C_n in 100 mL of 10 mm phosphatebuffered saline (PBS) with two different pH values (pH 5.7 and pH 7.4), which was then separated at regular intervals. The released MMC concentration in 10 mm PBS was determined by measuring absorbance at 360 nm and referenced to a standard curve, allowing the release rate of MMC loaded HMNPs- C_n for MMC can be calculated.

2.7 Preparation of Technetium-99m ($^{99}\text{Tc}^{\text{m}}$) labeled hollow magnetic nano-spheres (HMNPs- C_n) and biodistribution

HMNPs- C_n were used for $^{99}\text{Tc}^{\text{m}}$ labeling in order to study the effect of these encapsulation capabilities on the $^{99}\text{Tc}^{\text{m}}$. The radiolabeling of HMNPs- C_n was carried out using the reported method [23]. Briefly, 4.9 mCi of 100 μL sodium pertechnetate ($\text{Na}^{99}\text{Tc}^{\text{m}}\text{O}_4$) was mixed with 2 mL medical saline and 400 μL stannous chloride (SnCl_2) in a vial, which could reduce $^{99}\text{Tc}^{\text{m}}$ (VII) into $^{99}\text{Tc}^{\text{m}}$ (III) ions. Thereafter, 20 mg unlabeled HMNPs- C_n was poured into the reaction vial and was exposed to magnetic stirring for 30 min at room temperature.

It was found that $^{99}\text{Tc}^{\text{m}3+}$ ions could also be adsorbed on the inner cavity and outer mesopore by physical adsorption. The radiochemical purity of the labeled compound was checked with a Capintec CRC-15R external dose calibrator. The purified HMNPs- C_n - $^{99}\text{Tc}^{\text{m}}$ was dispersed in physiological saline to generate 20mg/2.5mL of labeled compound solution by supersonic treatment. The results of the labeling efficiency of $^{99}\text{Tc}^{\text{m}}$ by HMNPs- C_n are exhibited in Table 1.

To further investigate the biodistribution of HMNPs nanoparticles, 100 μl $^{99}\text{Tc}^{\text{m}}$ labelled HMNPs solution were injected into the female mice via caudal vein. After a certain time in magnetically targeted therapy, the treated female mice were scanned under single photoemission-computed tomography (SPECT) imaging. The animals were then sacrificed with an overdose of sodium pentobarbital; following the main organs (the blood, heart, lung, liver, spleen, pancreas, stomach, small intestine, large intestine, brain, muscle and bone matter) were detached and weighed. The main organs were finally rinsed with buffer and the remaining cell-associated radioactivity was measured with a γ -counter.

3. Results And Discussion

3.1 Characterization of hollow magnetic nano-spheres HMNPs- C_n

Fig. 3A(a) displays the $\alpha\text{-Fe}_2\text{O}_3$ nanoparticles spectrum, the diffraction peak intensity and position in $2\theta=30.3^\circ$, 35.6° , 43.3° , 53.7° , 57.3° , and 63.3° are consistent with the standard powder diffraction card (JCPDS 25-1402) for $\alpha\text{-Fe}_2\text{O}_3$, indicating that the prepared product is $\alpha\text{-Fe}_2\text{O}_3$. Two images of both HMNP- C_{16} and HMNP- C_{18} are recorded in Fig. 3A(b) and 3A(c), all show diffraction peaks in the position of $2\theta=30.2^\circ$, 35.5° , 43.2° , 53.8° , 57.3° , and 62.9° , and in agreement with the characteristic peaks of the PDF data (JSPDS 19-0629) for inverse spinel cubic phase Fe_3O_4 , demonstrating that the inorganic core of $\alpha\text{-Fe}_2\text{O}_3$ centered in HMNPs- C_n has been changed into the Fe_3O_4 . Both of HMNPs- C_{16} and HMNPs- C_{18} show broad diffraction peaks at the position of $2\theta=22^\circ$, which is a characteristic of amorphous SiO_2 nanoparticles, signifying that SiO_2 has been successfully coated on the surface of Fe_3O_4 .

The hollow magnetic nano-spheres HMNPs- C_{16} and HMNPs- C_{18} were characterized by IR respectively (Fig. 3B). The peaks around 574 cm^{-1} indicated the presence of Fe-O group, the asymmetric stretching and symmetric stretching of Si-O-Si were exhibited at 1097.2 cm^{-1} , 796 cm^{-1} and 467.1 cm^{-1} , respectively. In addition, the stretching vibrations of Si-OH groups at 957.5 cm^{-1} illustrated that higher surface area was occurred[24]. The stretching band at 1634 cm^{-1} may be attributed to the presence of residual physisorbed water molecules.

As can be observed from the EDS analysis results recorded in Fig. 3(C, D), both HMNPs- C_{16} and HMNPs- C_{18} only contain three elements Si, Fe and O, whose corresponding atomic ratios are 3.9:1:7 and 4.6:1:7 respectively, greater than that typical observed 1 : 2 for Si : O ratio in SiO_2 , and 3 : 4 in Fe_3O_4 . This is

owing to the fact that the oxygen atoms in Fe_3O_4 are able to coordinate to the Si atoms in the silica shell, in which the Si atom and the Fe atom share an oxygen atom to form a complex.

3.2 Transmission electron microscopy (TEM) analysis

$\alpha\text{-Fe}_2\text{O}_3$, b. $\alpha\text{-Fe}_2\text{O}_3@ \text{SiO}_2$, c. HMNPs-C₁₆, d. HMNPs-C₁₈

The $\alpha\text{-Fe}_2\text{O}_3$ nanoparticles synthesized by the reflux method are spherical (Fig. 4a). The average particle size measured by electronic scale is about 60 nm, with acceptable dispersion and clear boundaries. $\alpha\text{-Fe}_2\text{O}_3@ \text{SiO}_2$ synthesized using the modified Stöber method has apparent core-shell structure with a $\alpha\text{-Fe}_2\text{O}_3$ core around 60 nm and the SiO_2 coating of about 10 nm.

HMNPs-C₁₆ and HMNPs-C₁₈ are hollow spherical, have good dispersibility, and uniform particle size (Fig. 4c and Fig. 4d). The diameter of HMNPs-C₁₆ is about 117 nm. The core of Fe_3O_4 had a thickness of near 70 nm and the cavity thickness about 18 nm and silica shell having a thickness of 15 nm were clearly observed. The diameter of HMNPs-C₁₈ is 156 nm. It was clearly observed that the core of Fe_3O_4 had a thickness around 90 nm, a cavity thickness of 20 nm, and a silica shell thickness of 20.7 nm.

3.3 Scanning electron microscopy (SEM) analysis and particle size measurement by laser-diffraction-size analyzer

To further observe the surface features of the synthesized products, the effects of different chain lengths on the size of hollow magnetic nano-spheres were viewed by scanning electron microscopy (SEM) methods. It can be observed from Fig. 5 that, both HMNPs-C₁₆ and HMNPs-C₁₈ products all exhibit uniform particle size with good dispersion. HMNPs-C₁₆ indeed consists of a number of spherical particles from approximately 100 to 120 nm in diameter, less than that of HMNPs-C₁₈. As a contrast, HMNPs-C₁₈ also clearly displays spherical particles in the diameter range of 150~170 nm. The result of laser diffraction method also indicates the product of HMNPs-C₁₆ has a rather narrow size distribution, the size distribution of the HMNPs-C₁₆ centers around the range from 115.6 nm to 119.1 nm (Fig. 5). In a comparison of HMNPs-C₁₆, the size distribution of the HMNPs-C₁₈ centers within the range of 152.0 nm to 162.8 nm. The results of size distribution are in agreement with the TEM results.

3.4 Mesoporous and magnetic properties of hollow magnetic nano-spheres

In order to study the drug (MMC) loading and release properties of hollow magnetic nano-spheres with different cavity structures, the ASAP2405N adsorption analyzer was used to determine nitrogen

adsorption-desorption isotherms, from which the BET specific surface area was calculated by Brunauer-Emmett-Teller (BET) equation using the adsorption data in the relative pressure (p/p_0) range of 0.05–0.30. The pore volume and pore structure distribution of calcined HMNPs-C₁₆ and HMNPs-C₁₈ were obtained by the BJH method.

As can be seen from the nitrogen adsorption-desorption isotherms of HMNPs-C₁₆ and HMNPs-C₁₈ (Fig. 6A and B), both show the characteristics of the IV type isotherm in the IUPAC classification at the relative pressure of p/p_0 of 0.01~0.99, indicating the presence of mesopores. However, the adsorption isotherm of HMNPs-C₁₆ has a distinction from that of HMNPs-C₁₈, the adsorption curve of the former is convex upward at turning point of $p/p_0=0.3953$, demonstrating condensation of pores. However, in contrast, the adsorption curve of the latter is concave upward at a turning point of $p/p_0=0.8073$, demonstrating weak action between adsorbent and adsorbate [25].

The physisorption isotherm of HMNPs-C₁₆ and HMNPs-C₁₈ all show hysteresis loops. For the product of HMNPs-C₁₆, adsorption isotherm has mixed types of H₂ and H₁ hysteresis loop [26], desorption is at first rapid at near saturation but becomes much gradual at a relative pressure of about 0.9 (the “slope platform” of the isotherm). The two branches in the slope platform of isotherm remain nearly horizontal and parallel over a wide range of relative pressures between 0.45 and 0.9, and the desorption boundary curve converges to the adsorption isotherm at a relative pressure of about 0.45, indicating inkbottle type mesopores [27]. As reported by K Morishige [28], a hysteresis loop of type H₂ and a steep desorption branch for HMNPs-C₁₆ signifies disordered mesoporous materials.

In contrast, the adsorption isotherm of HMNPs-C₁₈ has a typical H₁ hysteresis loop [29], and the two branches in the isotherm remain nearly vertical and parallel between 0.80 and near saturation. The desorption boundary curve is not able to converge to the adsorption isotherm from the beginning to end, demonstrating cylindrical mesopores of uniform radius [29].

According to our previous work [22], the longer the surfactant chain lengths, the higher ordered the products, which brings about differences of mesoporous properties between HMNPs-C₁₆ and HMNPs-C₁₈. Accordingly, the longer dual-function surfactant C₁₈TMS can generate more micelles, enhancing interaction between silicates species and dual-function surfactant, thus favoring condensation of silicates species. As a template, the longer C₁₈TMS is able to direct the formation of HMNPs with higher ordered cylindrical mesopores and compact pore wall, while, in contrast, the shorter C₁₆TMS directs formation of HMNPs with disordered inkbottle type mesopores.

Fig. 6(C) shows pore size distribution of HMNPs-C₁₆ and HMNPs-C₁₈. The most probable pore diameter of HMNPs-C₁₈ was 2.40 nm according to BJH (Barrett-Joyner-Halenda) desorption model. Nitrogen adsorption/desorption experiments exhibited that the measured BET surface area was 106.19 m²/g, while the BJH pore volume was 0.675 cm³/g. In comparison with the HMNPs-C₁₈; the product of HMNPs-

C₁₆ had a a little bigger size than that of HMNPs-C₁₈, this is because capillary evaporation occurs via spontaneous cavitation of the condensed liquid in the

large cavities, when the cavity size is increased, the adsorption branch shifts into higher relative pressures[30]. Its most probable pore diameter was 2.63 nm, with a decrease in the BJH pore volume to 0.773 cm³/g, the calculated BET surface area decreased to 383.52 m²/g accordingly.

The magnetic properties of the HMNPs-C₁₆ and HMNPs-C₁₈ were investigated by a vibrating sample magnetometer (VSM BH-55) with fields up to 30 K Gauss at room temperature. The product of α -Fe₂O₃@SiO₂ reduced in 4 vol% H₂ in N₂ at 400 °C was also characterized by VSM. The M-H curves of products can be seen in Fig. 6(D).

The M-H curves of the α -Fe₂O₃@SiO₂ after H₂ reduction display strong saturation magnetization (Ms.) at 71.41 emu·g⁻¹ and with a minor residual magnetization of 1.45 emu/g, which can designate the transformation of α -Fe₂O₃ into Fe₃O₄.

The Ms. value of hollow magnetic nano-spheres HMNPs-C₁₆ and HMNPs-C₁₈ were 50.01 emu·g⁻¹ and 45.30 emu·g⁻¹, respectively—both had a very minor residual magnetization of about 0.65 emu·g⁻¹, and had a low coercivity around 28.60 Oe, characteristics of good soft magnetic properties. Therefore, both were easily collected by an external magnet, and gentle shaking could easily make them well-dispersed throughout the solution.

The magnetic properties between HMNPs-C₁₆ and HMNPs-C₁₈ were compared. The HMNPs-C₁₆ revealed a higher magnetization value than that of HMNPs-C₁₈; owing to the fact that HMNPs-C₁₈ had a thicker silica shell (21.5 nm) than that of HMNPs-C₁₆ (15 nm), a large shielding effect on magnetic properties of Fe₃O₄ was generated. In addition, based on the results of EDS analysis, a higher fraction of Fe atoms (8.32 %) in HMNPs-C₁₆ than that in HMNPs-C₁₈ (7.94 %) may lead to magnetic properties of HMNPs-C₁₆ being improved.

3.5 MMC loading efficiency and in vitro MMC release of HMNPs-C_n loaded MMC

As shown in Fig. 7a, the amount of MMC adsorbed on both HMNPs-C₁₆ and HMNPs-C₁₈ increased with increasing initial concentration of MMC. When the initial MMC concentration attained 250 mg/g (1000 μ g MMC/5 mg HMNPs), both adsorption curves were close to the saturated monolayer adsorption with the L shape of the curve exhibited, which revealed a type I curve for both adsorption curve in the BDDT classification, and was thus indicative of both open HMNPs-C₁₆ and HMNPs-C₁₈ framework with permanent microporosity. The findings are in agreement with the results shown in Fig. 6.

As shown in Fig. 7a, MMC loading efficiency of HMNPs-C₁₈ was lower than that of HMNPs-C₁₆ indicating the HMNPs-C₁₆ loaded larger amounts of MMC than that of the HMNPs-C₁₈. This is owing to the fact that the pore size, surface area, and pore volume of HMNPs-C₁₆ were larger than those of HMNPs-C₁₈.

The release rate of MMC on both HMNPs-C₁₆ and HMNPs-C₁₈ at different pH levels (pH 5.7 and 7.4) is shown in Fig. 8b. It can be observed that the MMC release rate gradually increased within the first 20 h, with the release rate reaching equilibrium after 50 h. Both HMNPs-C₁₆ and HMNPs-C₁₈ all showed a clear pH-dependent drug release behavior; the release rate of HMNPs-C₁₆-MMC and HMNPs-C₁₈-MMC drug was relatively slow at pH 7.4, and slowed down after 7 h with an initial release of about 17 % and 22 %, respectively. After 50 h, their equilibrium release reached 63 % and 72 % for HMNPs-C₁₆-MMC and HMNPs-C₁₈-MMC, respectively.

In contrast, the release of the two hollow nano-spheres in 10 mM PBS solutions at a pH level of 5.7 was much faster, and also approximately 75 % and 81 % of the drug was released in the 10 mM PBS solution at a pH level of 5.7 for HMNPs-C₁₆-MMC and HMNPs-C₁₈-MMC drug, respectively, after 50 h. Drugs and hollow nano-spheres carry a positive charge at a lower pH, providing the necessary exclusion between them. These factors are the main drivers of drug release in acidic environments.

3.6 Drug diffusion mechanism of HMNPs-C_n loaded MMC

As can be seen from Fig. 8a, on account of their mesoporous SiO₂ thin shell and a cavity of size about 65 nm, hollow magnetic nanoparticles act as a capsule for drug molecule storage. MMC is uniformly loaded in the cavity of HMNPs-C_n; when the MMC loaded HMNPs-C_n was dispersed in the normal 10 mM PBS solutions, both adsorption and desorption took place in a reversible kinetic model.



As the MMC loaded HMNPs-C_n desorbed MMC into PBS solutions, the drug release was unavoidably controllable in two stages attributable to relatively rapid initial diffuse from outer surface adsorption, and slower permeation from inner void through cavities. It is worth mentioning, that a residual amount of the drug remained left within the cavity of HMNPs-C_n. This is owing to the fact that HMNPs-C_n possessed circular voids and a mesoporous shell; having strong specific adsorption ability to MMC molecules, it will take some time to reach the adsorption-desorption equilibrium. An experiment was designed to verify this fact. Though the solution remained clear before release of MMC, the solution changed to purple after the release of MMC, fully demonstrating that the diffusion of MMC into PBS solutions from MMC loaded HMNPs-C_n was spontaneous.

Once the MMC molecules diffuse through HMNPs-C_n hollow spheres, they then diffuse through the diffusion layer. Thus the drug release could be controlled by the diffusion through the HMNPs-C_n hollow spheres or by the diffusion through the solution layer surrounding the hollow spheres. The release rate of drug molecules would be determined by the slower step of these two processes. Bhaskar et al. [31] developed a simple procedure to establish whether or not the diffusion through the particle was the rate limiting step. For a particle diffusion-controlled release, Bhaskar et al. [31] obtained the following equation:

$$\ln(1-X_t) = -1.59(6/d_p)^{1.3}D^{0.65}t^{0.65}$$

where d_p is particle diameter, and D is the diffusivity. This suggests that particle diffusion control can be tested by simply testing for linearity between $\log(1-X_t)$ and $t^{0.65}$. This method was applied to the experimental data, and a suitable linear relationship (correlation coefficient $R^2 \geq 0.9760$) was obtained for the pH 5.7 and 7.4 release respectively (see Fig. 8b), indicating that for these two pH releases, the diffusion through both HMNPs-C₁₆ and HMNPs-C₁₈ hollow spheres is the rate limiting step.

3.7 In vitro release kinetics of HMNPs loaded with MMC

According to L Xu [32], the slow release kinetics of HMNPs-C₁₈ and HMNPs-C₁₆ on MMC can be treated using pseudo-first-order and pseudo-second-order models. The pseudo-first-order rate expression can be written as: ; here, Q_t means the release amount of MMC (%) at time t (h), Q_e refers to the release amount of MMC when balancing (%), and k_1 is the release rate constant (1/h).

The pseudo-second-order model rate expression can be written as:

$$\frac{t}{Q_t} = \frac{1}{k_2 Q_e^2} + \frac{1}{Q_e} t$$

In the equation, k_2 refers to the release rate constant (1/h).

With the simulation of the above two kinetic models for release kinetic data, it was found that the pseudo-first-order is more satisfactory for describing the release kinetic process of MMC from HMNPs-C₁₆-MMC composites than that of the pseudo-second-order. Fig. 9a shows the plot of $\log(Q_e - Q_t)$ vs. t for the release of MMC at pH 5.7 and 7.4 environments, respectively, and as can be seen, fair straight lines were obtained. For the pH 5.7 release, the correlation coefficient (R^2) and k_1 values are 0.9897 and 0.06944 h⁻¹, respectively, and for the pH 7.4 release, they are 0.9924 and 0.05790 h⁻¹, respectively. The release kinetics result is not similar to the HMNPs-C₁₈-MMC composites, for which, pseudo-second-order is more satisfactory. Fig. 10 b shows the plot of t/Q_t vs. t for the release of MMC at pH 5.7 and 7.4 environments,

respectively, and as can be seen, fair straight lines were obtained. For the pH 5.7 release, the correlation coefficient (R^2) and k_2 values are 0.9976 and 0.002093 h^{-1} , respectively, and for the pH 7.4 release, they are 0.9977 and 0.001173 h^{-1} , respectively.

The difference between of HMNPs- C_{16} -MMC and HMNPs- C_{18} -MMC composites in release kinetics results from the different pore structures of HMNPs- C_{16} and HMNPs- C_{18} . In the adsorption-desorption equilibrium, the surface charge of sorbents and hydrogen bonding between the groups of MMC and the silanol groups packed on the pore wall may be the chief force to hold MMC molecules in HMNPs- C_n hollow spheres. The interaction between two materials and MMC molecules is different, resulting in different release kinetics [32].

In contrast to HMNPs- C_{16} , the faster release of HMNP- C_{18} was actually related to the weaker interaction with MMC molecules. HMNPs- C_{16} has disordered inkbottle type mesopores with an open pore diameter of about 2.63 nm. When HMNPs- C_{16} was used as a vehicle to encapsulate the MMC drug, the drug was not arranged in a crystalline form on account of space confinement [33]. When confined to the narrow pores, and disordered inkbottle pore space, MMC molecules were prevented from arranging themselves into a crystal lattice. Consequently, once release of MMC out of the inkbottle pore space occurs, it may take a “vacancy” state, which is consistent with the pseudo-first-order model. Fig. 8b exhibits that, no matter what pH condition, HMNPs- C_{16} -MMC composites have lower release percentages of MMC in the first 30 min, implying that the disordered inkbottle pore space of HMNPs- C_{16} can prevent leaching of the loaded MMC molecules before the HMNPs- C_{16} -MMC were taken up by cells. This is another advantage of using HMNPs- C_{16} as drug vehicles for intracellular drug delivery applications. In current work, HMNPs- C_{16} was considered to be an optimum preparatory radioactively labeled vehicle.

3.8 Labeling efficiency and Technetium- $^{99m}\text{Tc}^m$ labeled HMNPs- C_n

Table 1

Our data for ^{99m}Tc -labelled HMNPs- C_n

Stay ^{99m}Tc -labelled	Initial activity of $\text{Na}^{99}\text{Tc}^m\text{O}_4$	Syringe's residual activity	Activity in wash fluids, clear liquor	^{99m}Tc -labelled HMNPs	Labeling efficiency
HMNPs- C_{16}	4.90 mCi	0.28 mCi	2.70mCi	1.30 mCi	30.4%
HMNPs- C_{18}	4.90 mCi	0.28 mCi	2.65mCi	1.35mCi	31.5 %

From Table 1, the labeling efficiency of magnetic hollow spheres HMNPs-C₁₈ and HMNPs-C₁₆ were calculated as 31.5% and 30.4% respectively; both considering 4.90 mCi ⁹⁹Tc^m decay to 4.28 mCi in the experiment. In comparison with the results of Zhang et al. [34] by complexation labeling of ⁹⁹Tc^m with DTPAA, the current work exhibits low the labeling efficiency of ⁹⁹Tc^m. This is ascribed to the fact that the issues of ⁹⁹Tc^m labeled HMNPs-C_n were involved in both cavity physical adsorption and the thermodynamic equilibrium. Therefore, it is necessary for ⁹⁹Tc^m labeled HMNPs-C_n to reach the equilibrium for a long enough time. Once the equilibrium of physical adsorption is reached, the ⁹⁹Tc^m labeled HMNPs-C_n reaches saturation, and so HMNPs-C_n chose to no longer continue labelling additional ⁹⁹Tc^m.

Table 1 shows that the ⁹⁹Tc^m-labeling efficiency of HMNPs-C₁₈ is higher than that of HMNPs-C₁₆; Although the ⁹⁹Tc^m-labeling efficiency of magnetic hollow spheres HMNPs-C_n is relatively low, the ⁹⁹Tc^m-labeling efficiency by physical adsorption can completely achieve the radiation intensity required for in vivo targeting of functional magnetic anticancer drug by using conventional isotopic tracer method [35-36].

Employing ⁹⁹Tc^m labeled magnetic HMNPs-C_n is a novel, simple and convenient route. For this reason, ⁹⁹Tc^m labeled HMNPs-C_n by physical adsorption can immediately be delivered into ICR mice via tail vein injection to observe in vivo targeting distribution of magnetic anticancer drug with the addition of magnetic targeting. The route for complexation labeling of ⁹⁹Tc^m with DTPAA is a lengthy and complicated method, requiring not only amino functionalization of magnetic hollow spheres, but also mono-coupling with diethylenetriaminepentaacetic acid (DTPAA). Therefore, ⁹⁹Tc^m labeled HMNPs-C_n by simple physical adsorption has the advantages of convenient and rapid quantification and localization in vivo.

3.9 HMNPs-C₁₆ targeting in vivo

Due to the wide distribution of each labelled hollow magnetic spheres throughout the body after the injection of HMNPs-C₁₆-⁹⁹Tc^m, high levels of radioactivity accumulation were observed in the liver, spleen, lung, and bladder after 2 h post injection, with a small amount of radioactive particles uptaking in the kidney (Fig. 10a). The results show that the ⁹⁹Tc^m labelled HMNPs-C₁₆ spheres can successfully break through the pulmonary circulation, and can be excreted through the urinary system. Instead, the HMNPs-C₁₆-⁹⁹Tc^m spheres were swallowed by the reticuloendothelial system (lung, liver and spleen).

In order to explore the targeting properties of ⁹⁹Tc^m labelled HMNPs-C₁₆-⁹⁹Tc^m spheres, the tumors of nude mice were placed on the magnetic pole of the YMC-11 medical pulse magnetic field generator with the output voltage of pulsed magnetic fields being controlled at 700 V for 2h. In the Fig. 10 b, the right

forelimb (A) is normal, the left forelimb (B) is the tumor region with targeting, the left hind limb (C) is the tumor region with no targeting and the right hind limb (D) is a sense of inflammation.

Fig. 10b shows nude mice SPECT imaging targeting for limb after injection. The intensive distribution of black dots in the image correspond to the large amount of $^{99}\text{Tc}^m$ labelled HMNPs-C₁₆- $^{99}\text{Tc}^m$ spheres that were accumulated into the tumor sites by a combination of passive magnetic targeting and active targeting mechanisms. In comparison with in vivo bio-distribution of $^{99}\text{Tc}^m$ labelled HMNPs-C₁₆ spheres, the targeting SPECT imaging showed the activity concentration of $^{99}\text{Tc}^m$ labelled HMNPs-C₁₆ spheres in the tumors were significantly higher than that without targeting, the experimental data of $B_{\text{tumor targeting}}/A_{\text{normal}}$ at 3.19 and $C_{\text{tumor no targeting}}/A_{\text{normal}}$ at 1.58 demonstrated these facts. In addition, the experimental data of $C_{\text{tumor no targeting}}/A_{\text{normal}}$ at 1.58 demonstrated that $^{99}\text{Tc}^m$ labelled HMNPs-C₁₆ spheres tended to accumulate in the tumor sites in vivo, implying $^{99}\text{Tc}^m$ labelled HMNPs-C₁₆ spheres have a good affinity to the tumor.

Table 2 shows the results of magnetically targeted radiotherapy employed $^{99}\text{Tc}^m$ labelled HMNPs-C₁₆ spheres. The liver uptake of $^{99}\text{Tc}^m$ labelled HMNPs-C₁₆ spheres was 14.6915, 19.2382, 28.9201, 38.0013 and 35.6282% ID/g at 15, 30, 60, 120 and 180 min respectively. The radioactivity in the spleen was 33.2598, 43.5203, 89.0264, 121.0420 and 69.2384% ID/g at 15, 30, 60, 120 and 180 min, respectively. The results showed HMNPs-C₁₆ had the highest spleen uptake of $^{99}\text{Tc}^m$ for 180 min after the injection; when the absolute organ uptake was compared, uptake by the lung was the second highest, and uptake by the liver was the third highest. The findings were in agreement with SPECT imaging data with high levels of $^{99}\text{Tc}^m$ labelled HMNPs-C₁₆ spheres uptake in the liver, spleen and lung. Furthermore, 4.7836 % of radioactive particle uptake was found in the bone for 180 min after the injection, indicating the $^{99}\text{Tc}^m$ labelled HMNPs-C₁₆ spheres were able to gradually accumulate in the bone with the lapse of time. On the contrary, relatively low radioactivity uptake was observed in the pancreas, brain, and muscle. This is likely because $^{99}\text{Tc}^m$ labelled HMNPs-C₁₆ spheres were rapidly cleared by the pancreas, brain, and muscle, and excreted by the mouse through the urine.

Table. 2

Biodistribution of $^{99}\text{Tc}^m$ labelled HMNPs-C₁₆ spheres in mice (% ID/g)

tissues	15 min	30 min	60 min	120 min	180 min
blood	1.5902	1.2601	1.4781	2.9036	2.1559
heart	1.4823	1.4601	2.5705	2.0721	1.6591
lung	54.0404	54.5706	67.6554	60.4534	60.3154
kidney	3.2623	4.2060	5.9933	10.3055	9.9447
liver	14.6915	19.2382	28.9201	38.0013	35.6282
spleen	33.2598	43.5203	89.0264	121.0420	69.2384
pancreas	0.4632	0.6518	0.7561	0.9074	0.7151
stomach	1.0481	1.3038	2.4930	2.4035	2.4406
small intestine	1.0231	1.1407	1.5061	1.9020	1.4596
large intestine	0.6202	0.8649	1.2040	1.6369	1.5288
brain	0.0609	0.0504	0.0776	0.1105	0.1240
muscle	0.2601	0.3416	0.3484	0.4480	0.4244
bone	1.6718	2.2664	3.8863	5.3645	4.7836

3.10 In vitro cytotoxicity against HeLa cells of HMNPs-C₁₆ spheres

The in vitro cytotoxicity against HeLa cells was investigated to evaluate the potential application for HMNPs-C₁₆ spheres as a drug carrier (Fig.11). HMNPs-C₁₆ spheres were selected as the model, and the results show that a 24 h and 48 h incubation of HeLa cells with different concentrations of sample with 0, 25, 50, 100, 150, and 200 $\mu\text{g mL}^{-1}$. The results indicate that HMNPs-C₁₆ spheres show no cytotoxicity to the HeLa cells with different concentrations. Even though the concentration of sample reached up to 200 $\mu\text{g mL}^{-1}$, the surviving fraction of HeLa cells is still up to 91 % for 24 h and 90 % for 48 h, indicating that HMNPs-C₁₆ spheres have relatively good biocompatibility.

4. Conclusion

In summary, the hollow magnetic nano-spheres of both HMNPs-C₁₆ and HMNPs-C₁₈ were synthesized and directed by dual-function template. The long alkyl chain n-octadecyl Trimethoxysilane directed assembly of HMNPs-C₁₈ with the size of 160 nm, and the short alkyl chain n-hexadecyl Trimethoxysilane directed assembly of HMNPs-C₁₆ with the size of 119 nm, demonstrating our proposed synthesis

strategy. On account of large surface area and pore volume, HMNPs-C₁₆ has higher MMC loading efficiency. A good linearity between $\log(1-X_t)$ and $t^{0.65}$ was found for both HMNPs-C₁₆ and HMNPs-C₁₈, demonstrating the diffusion through hollow magnetic nano-spheres was the rate limiting step. MMC drugs can be efficiently loaded into the hollow magnetic nano-spheres HMNPs-C_n, and be released through acid-assisted diffusion/dissolution controlled kinetics. Release kinetics of the HMNPs-C₁₈-MMC was well described by pseudo-second-order equation, but pseudo-first-order was more satisfactory for release kinetics of HMNPs-C₁₆-MMC. This is owing to the fact that HMNPs-C₁₈ had ordered cylindrical mesopores, while HMNPs-C₁₆ had disordered inkbottle pores, which could potentially prevent leaching of the loaded MMC molecules before they were taken up by cells. Accordingly, as an optimum vehicle, HMNPs-C₁₆ hollow spheres exhibited a relatively high saturation magnetization (50.01 emu·g⁻¹) and could be labeled with radioisotope ⁹⁹Tc^m. This allowed ⁹⁹Tc^m labelled HMNPs-C₁₆ to be injected into the mice to study the biodistribution of magnetic nanoparticles in different organs, and the results, as well as MTT assays, revealed that HMNPs-C₁₆ spheres have relatively acceptable biocompatibility, and were found to accumulate in the spleen, lung, liver, and bone matter, showing obvious magnetic targeting effects.

Declarations

Conflict interests

The authors have no relevant financial or non-financial interests to disclose.

Funding

This work was supported by the National Natural Science Foundation of China (20577010, 20971043), the Fundamental Research Funds for the Central Universities, and the Open Project Program of State Key Laboratory of Inorganic Synthesis and Preparative Chemistry, Jilin University.

References

1. M. Sastry, R. Fiala, R. Lipman, M. Tomasz, D.J. Patel, *J. Mol. Biol.* **247**, 247-338 (1995)
2. A.C. Sartorelli, W.F. Hodnick, M.F. Belcourt, M. Tomasz, B. Haffty, J.J. Fischer, S. Rockwell, *Oncol. Res.* **6**, 501-508 (1994)
3. M. Öno, Z. Aktaş, B. Hasanreisoglu, *Clin. Experiment. Ophthalmol.* **36**(4), 316-322 (2008)
4. Y. Zhu, W.G. Lu, L.Y. Zou, J.F. Feng, *Chin. J. Pharm.* **37**(3), 168-171 (2006)
5. M.E. Sharifabad, T. Mercer, T. Sen, *J. Appl. Phys.* **117**(17), 17D139 (2015)
6. L. Yuan, X.R. Qi, *Chin. J. New Drugs* **17**(3) 217-224, 227 (2008)
7. N.K. Mal, M. Fujiwara, Y. Tanaka, *Nature* **421**, 350-353 (2003)
8. V.-R. María, B. Francisco, A. Daniel, *Angew. Chem. Int. Ed.* **46**(40) 7548–7558 (2007)

9. L. Zhang, T. Wang, L. Yang, C. Liu, C. Wang, H. Liu, Y.A. Wang, Z. Su, *Chem. Eur. J.* **18**(39), 12512–12521 (2012)
10. J. Liu, S.Z. Qiao, S.B. Hartono, G.Q. Lu, *Angew. Chem. Int. Ed.* **49**(29) 4981–4985 (2010)
11. P.B. Santhosh, N.P. Ulrih, *Cancer Lett.* **336**(1), 8–17 (2013).
12. W. Zhao, J. Gu, L. Zhang, H. Chen, J. Shi, *J. Am. Chem. Soc.* **127**, 8916–8917 (2005)
13. S.I.U. Madrid, U. Pal, Y.S. Kang, J. Kim, H. Kwon, J. Kim, *Nanoscale Res. Lett.* **10**, 1-8 (2015)
14. C. Cannas, E. Musu, A. Musinu, G. Piccaluga, G. Spano, *J. Non-Cryst. Solids* **345-346**, 653–657 (2004)
15. R. Purbia, S. Paria, *Nanoscale* **7**, 19789–19873 (2015)
16. L. Zhang, S.Z. Qiao, Y.G. Jin, Z.G. Chen, H.C. Gu, G.Q. Lu, *Adv. Mater.* **20**, 805–809 (2008)
17. J.J. Yuan, X. Zhang, H. Qian, *J. Magn. Mag. Mater.* **322**(15), 2172-2176 (2010)
18. Y.F. Zhu, E. Kockrick, T. Ikoma, N. Hanagata, S. Kaskel, *Chem. Mater.* **21**, 2547–2553 (2009)
19. J. Zhou, W. Wu, D. Caruntu, M. H. Yu, A. Martin, J. F. Chen, C. J. O'Connor, W. L. Zhou, *J. Phys. Chem. C.* **111**, 17473–17477 (2007)
20. W. Zhao, H. Chen, Y. Li, L. Li, M. Lang, J. Shi, *Adv. Funct. Mater.* **18**(18), 2780–2788 (2008)
21. J. Zhang, C.Q. Lan, M. Post, B. Simard, Y. Deslandes, T.H. Hsieh, *Cancer Genom. Proteom.* **3**(3-4), 147–158 (2006)
22. Y.X. Yang, H.P. Ying, J.G. Shao, *J. Am. Ceram. Soc.* **90**(11), 3460–3467 (2007)
23. S.Q. Shah, M.R. Khan & S.M. Ali, *Nucl. Med. Mol. Imaging* **45**, 248-254 (2011)
24. Y. Chen, H. Chen, L. Guo, Q. He, F. Chen, J. Zhou, J. Feng, J. Shi, *ACS Nano.* **4**(1), 529–539 (2010)
25. J.M. Yan, Q. Zhang, J.C. Gao, Beijing Science Press 115 (1986)
26. K.S.W. Sing, R.T. Williams, *Adsorpt. Sci. Technol.* **22**(10), 773-782 (2004)
27. W.D. Xiang, Y.X. Yang, J.L. Zheng, *Mater. Science-Poland* **28**(3), 709-730 (2010)
28. K. Morishige, M. Tateishi, F. Hirose, K. Aramaki, *Langmuir* **22**(22), 9220-9224 (2006)
29. J.B. Zhang, Y.X. Yang, J.L. Zheng, *Chin. J. Inorg. Chemistry* **27**(9), 1817-1829 (2011)
30. K. Morishige, N. Tateishi, *J. Chem. Phys.* **119**(4), 2301-2306 (2003)
31. R. Bhaskar¹, R.S.R. Murthy, B.D. Miglani, K. Viswanathan, *Int. J. Pharm.* **28**(1), 59–66 (1986)
32. L. Xu, J. Dai, J. Pan, X. Li, P. Huo, Y. Yan, X. Zou, R. Zhang, *Chem. Eng. J.* **174**, 221– 230 (2011)
33. Y. Hua, Z. Zhi, Q. Zhao, C. Wu, P. Zhao, H. Jiang, T. Jiang, S. Wang, *Microporous Mesoporous Mater.* **147**(1), 94–101 (2012)
34. J.X. Zhang, Q. Zhang, A.D. Huang, *J. Instrum. Analysis* **22**(3), 69-71 (2003)
35. M.C.F. Passos, C.F. Ramos, M. Bernardo-Filho, D.M.M. De Mattos, E. G. Moura, *Nucl. Med. Commun.* **21**(11), 1059-1062 (2000)
36. X. Xie, S. Deng, *Nucl. Techniques* **11**, 011 (2005)

Figures

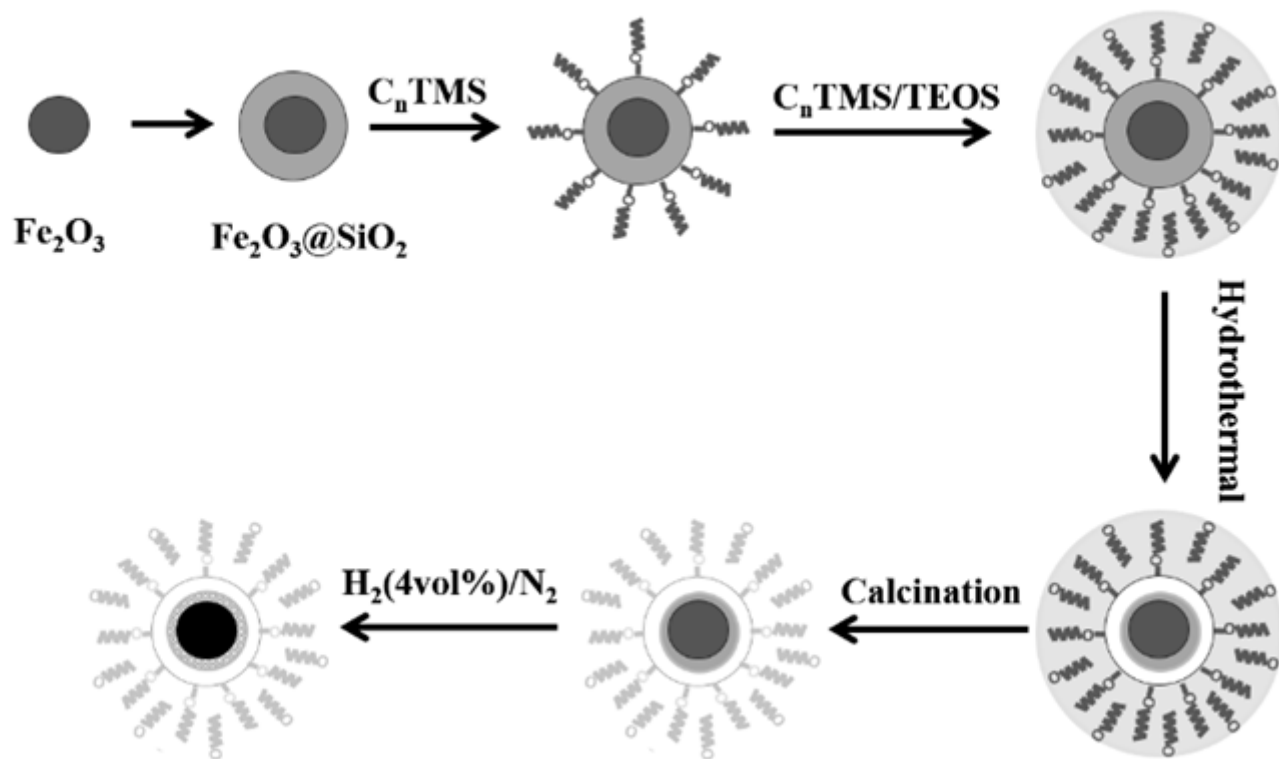


Figure 1

Scheme of the synthetic procedure of HMNPs ($\text{Fe}_3\text{O}_4@\text{SiO}_2@\text{C}_n\text{TMS}$)

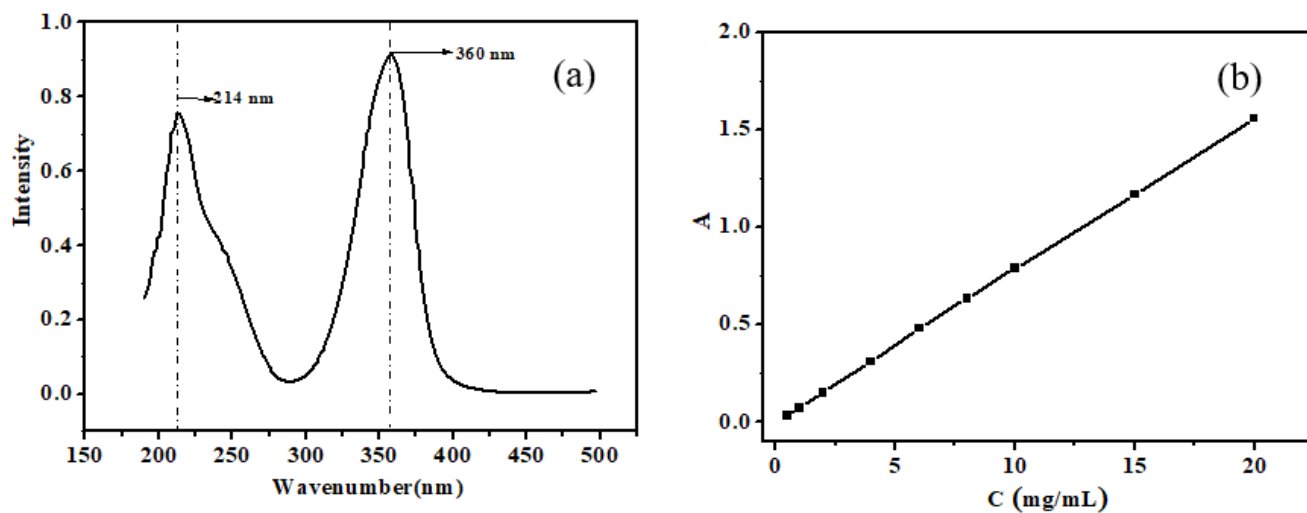


Figure 2

Ultraviolet absorption spectrum of MMC (a); Standard curve of the free MMC concentration response to absorbance at 360 nm (b)

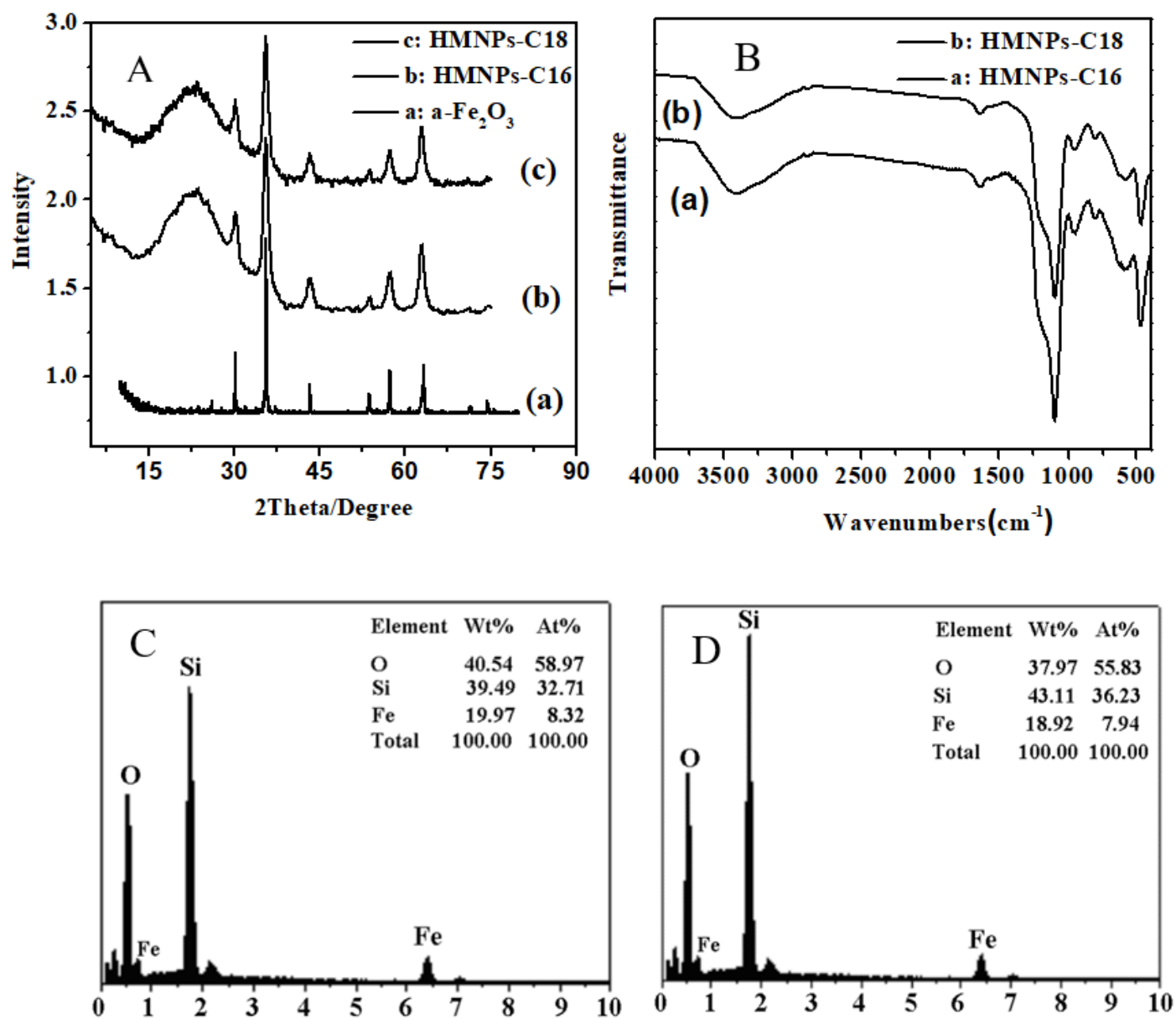


Figure 3

(A)XRD patterns and (B) IR Spectra and EDS images of HMNPs-C₁₆ (C); HMNPs-C₁₈ (D)

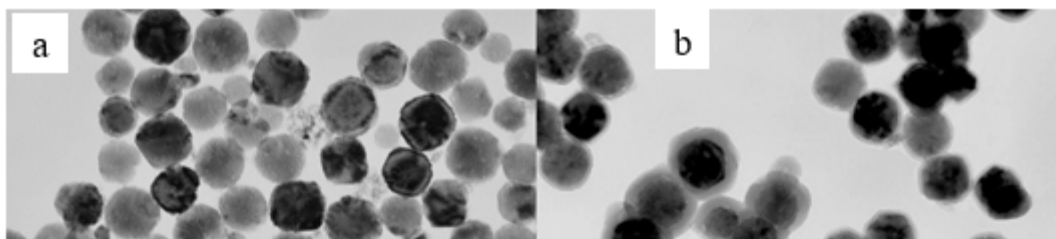


Figure 4

TEM image of $\alpha\text{-Fe}_2\text{O}_3$, $\alpha\text{-Fe}_2\text{O}_3\text{@SiO}_2$ and hollow magnetic nano-spheres

$\alpha\text{-Fe}_2\text{O}_3$, b. $\alpha\text{-Fe}_2\text{O}_3\text{@SiO}_2$, c. HMNPs-C₁₆, d. HMNPs-C₁₈

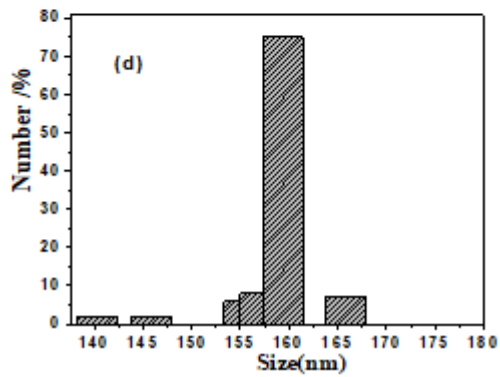
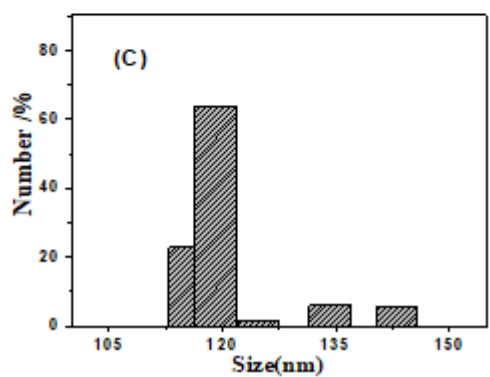
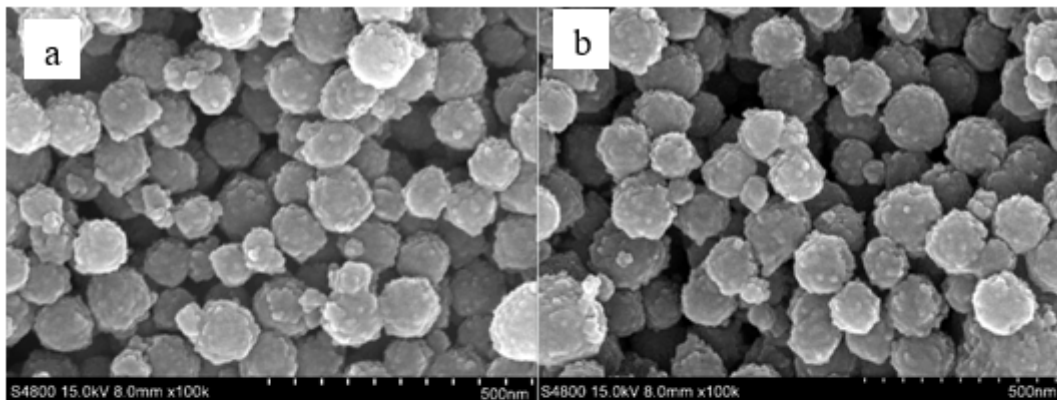


Figure 5

SEM image of HMNPs-C₁₆ (a), HMNPs-C₁₈ (b) and HMNPs-C₁₆ (c), HMNPs-C₁₈ (d) nanoparticles size distribution

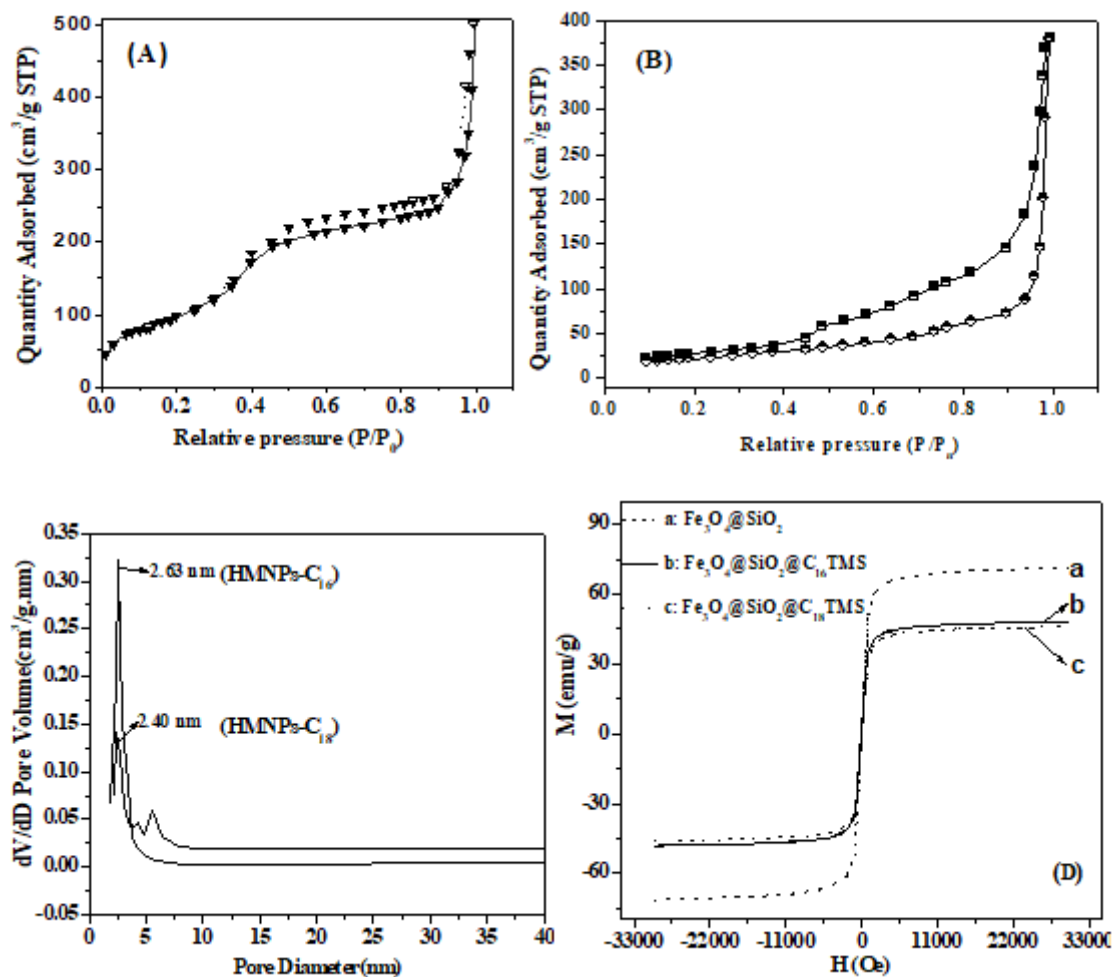


Figure 6

Mesoporous and magnetic properties of HMNPs, Low temperature N_2 adsorption-desorption isotherm curve of HMNPs- C_{16} (A) and HMNPs- C_{18} (B), pore size distribution of HMNPs(C) and magnetization curve of products (D)

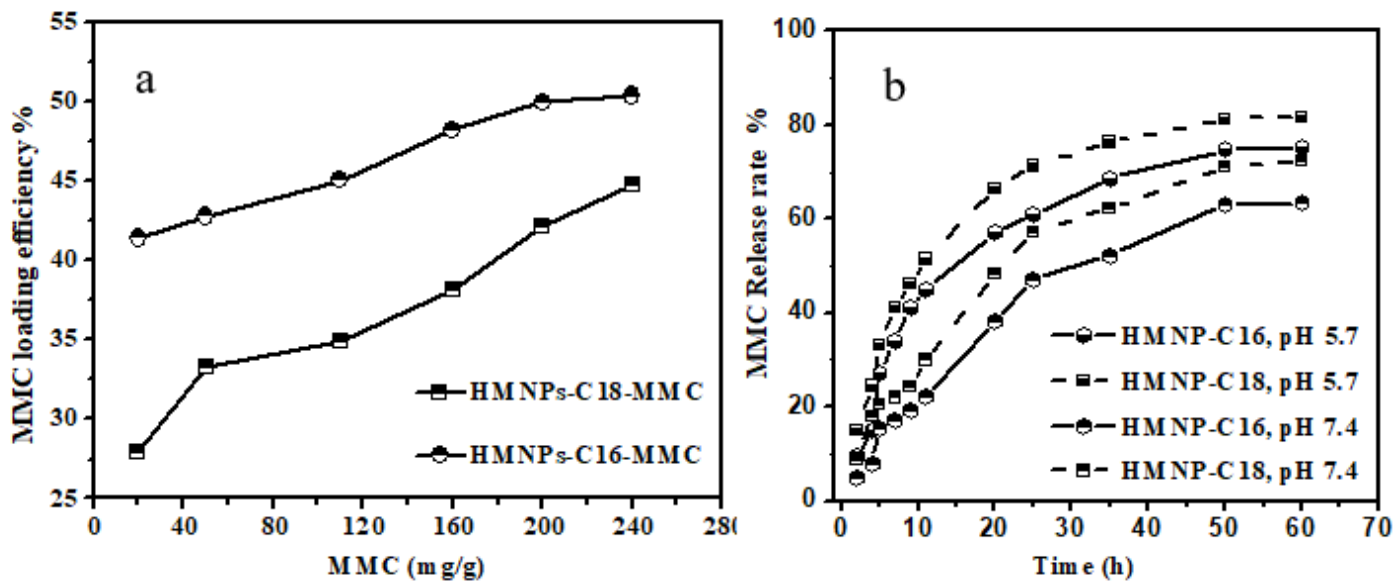


Figure 7

MMC adsorption curve of HMNPs-C_n in 10 mM PBS (pH 7.4) and MMC release of HMNPs-C_n in 10 mM PBS (pH 5.7 and 7.4)

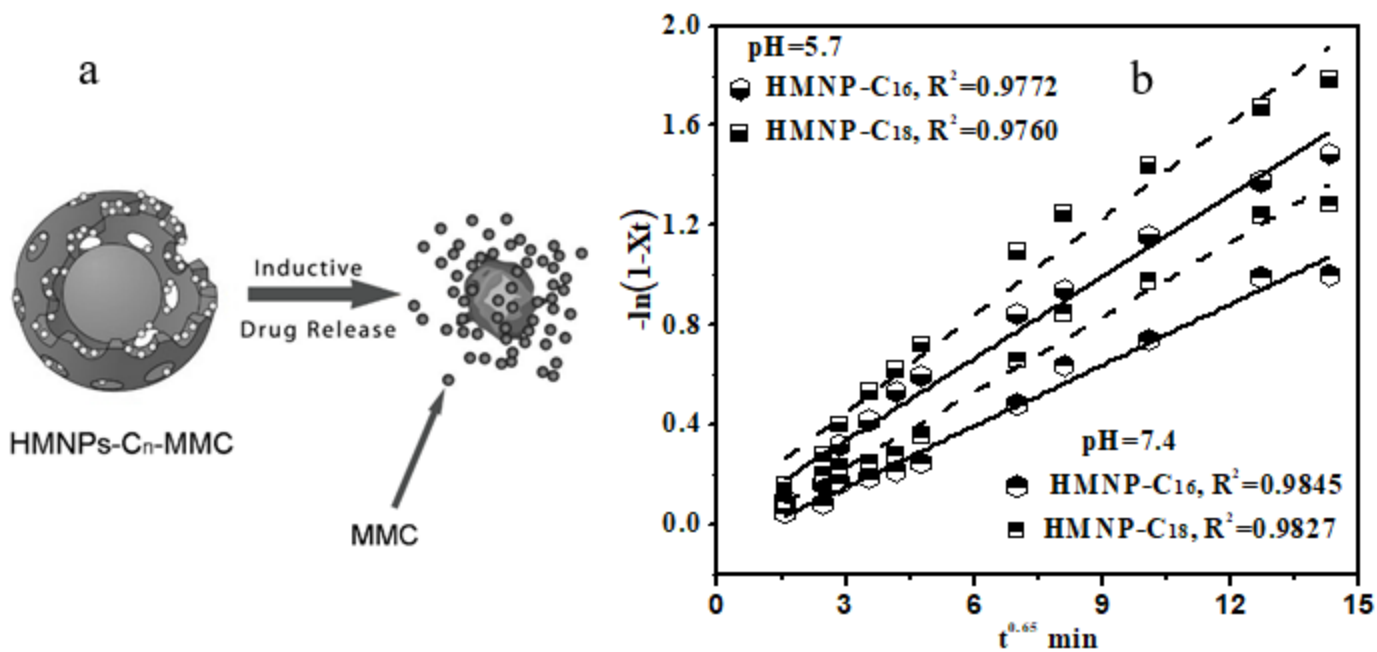


Figure 8

Scheme (a) for release of MMC from HMNPs-C₁₆-MMC composites and (b) with $-\log(1-X_t)$ as a function of $t^{0.65}$ in PBS solution (pH 7.4 and pH 5.7)

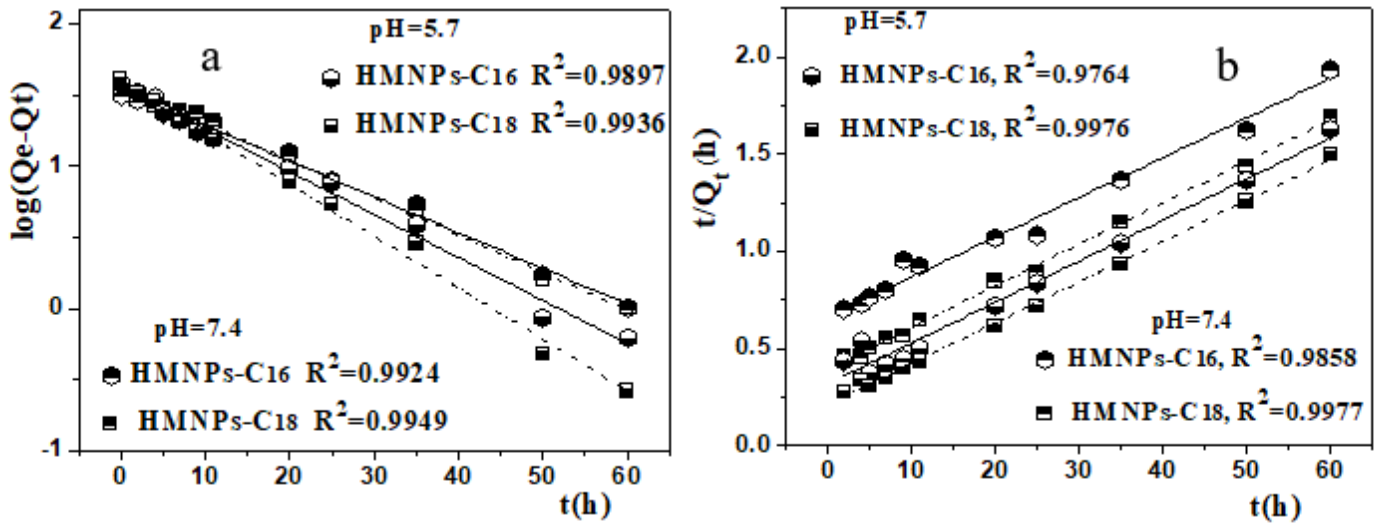


Figure 9

Pseudo-first-order (a) and pseudo-second-order (b) of MMC release processes in the PBS (pH 5.7 and 7.4) from both HMNPs-C₁₆ and HMNPs-C₁₈

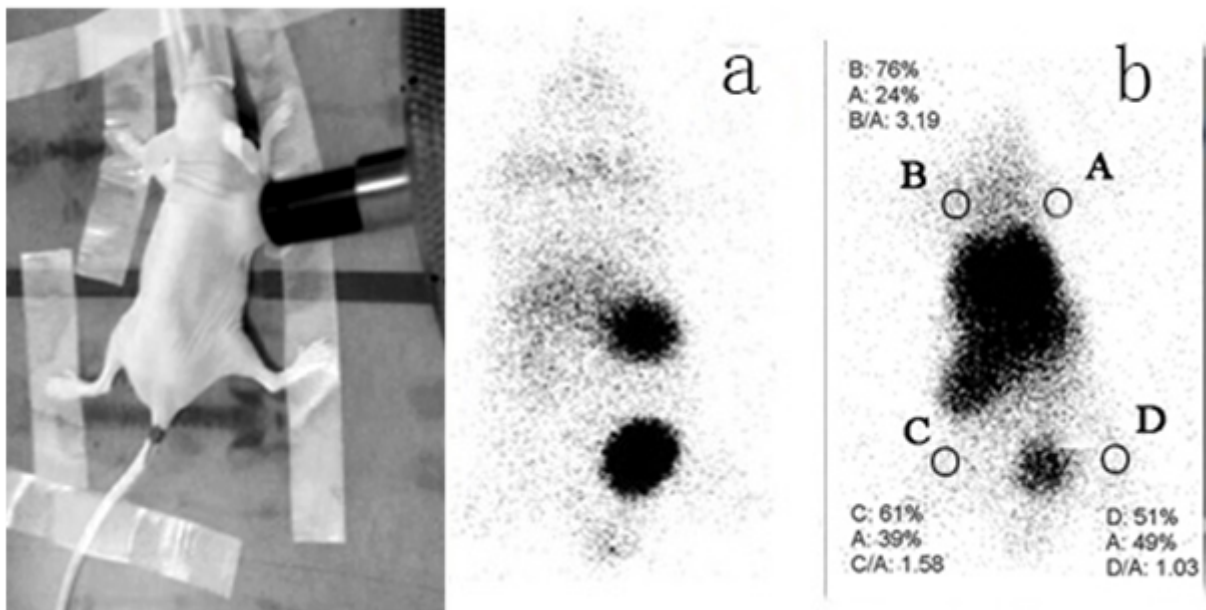


Figure 10

The SPECT images of the mouse after injection with HMNPs-C₁₆-^{99m}Tc spheres by (a) no targeting and (b) targeting.

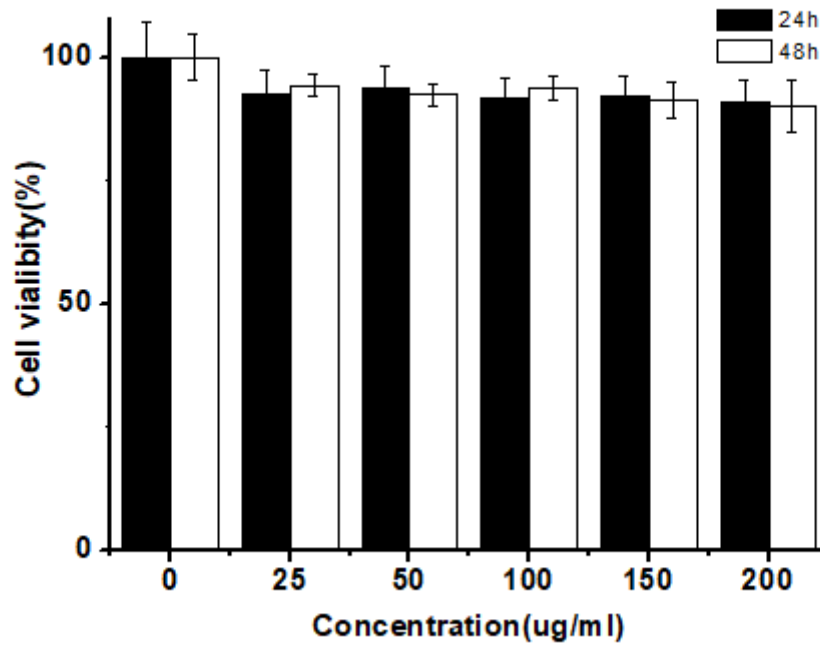


Figure 11

Cell viabilities of HeLa cells after incubation with different concentrations of HMNPs-C₁₆ spheres for 24 and 48 h.

Supplementary Files

This is a list of supplementary files associated with this preprint. Click to download.

- [GraphicalAbstract.docx](#)
- [highlights.docx](#)